Research Article

Sandhya Ravichandran, Bipul K. Mahato, Jaivardhan Sinha, Rajdeep Singh Rawat, Hettiarachchige Chamanei Sandamali Perera, Arnab Ganguly*, and Gobind Das*

Impact of surface and configurational features of chemically synthesized chains of Ni nanostars on the magnetization reversal process

https://doi.org/10.1515/ntrev-2025-0223
received June 12, 2025; accepted September 12, 2025

Abstract: Magnetic nanoparticles and nanochains hold significant importance in data storage and biomedical applications due to their small size, high aspect ratio, and distinctive reversal properties. However, these properties are significantly affected by the surface morphology and fine orientational features of the particles. This study systematically examines the magnetic reversal and hysteretic properties of Ni nanostar-chains and their constituent particles, focusing on the surface characteristics and geometric configurations resulting from chemical synthesis. The investigation reveals the influence of surface roughness, manifested as spikes, on the reversal landscape. Additionally, it delves into the impact of structural properties of self-assembled nanochain clusters on the reversal behaviour. The findings offer valuable insights into fundamental magnetic phenomena in chemically synthesized magnetic nanostructures, emphasizing their morphological and geometric characteristics. This approach details minute features of nanostructures, paving the way for advancements in computer memory and biotechnology applications.

Keywords: nanoparticles, magnetization reversal, Mumax^3

*** Corresponding author: Arnab Ganguly**, Department of Physics and Nanotechnology, SRM Institute of Science and Technology, Kattankulathur, 603203, Tamil Nadu, India, e-mail: arnabg@srmist.edu.in
*** Corresponding author: Gobind Das,** Department of Physics, Khalifa University, Abu Dhabi, United Arab Emirates; Center for Catalysis and Separation (CeCas), Khalifa University, Abu Dhabi, United Arab Emirates, e-mail: gobind.das@ku.ac.ae
Sandhya Ravichandran, Jaivardhan Sinha: Department of Physics and Nanotechnology, SRM Institute of Science and Technology, Kattankulathur, 603203, Tamil Nadu, India
Bipul K. Mahato, Rajdeep Singh Rawat: Natural Sciences and Science Education, National Institute of Education, Nanyang Technological University, 1 Nanyang Walk, Singapore, 637616, Singapore
Hettiarachchige Chamanei Sandamali Perera: Department of Physics, Khalifa University, Abu Dhabi, United Arab Emirates

1 Introduction

In the field of nanoscience, metallic nanomaterials are substances that display remarkable physical properties at the nanoscale, generally measuring from a few nanometres to several hundred nanometres. Their unique characteristics, especially their intrinsic magnetic [1,2] and plasmonic [3,4] properties, have gained considerable interest and opened up promising applications in various fields [5,6]. Recent advancements in nanomaterial synthesis and nanofabrication techniques have enabled the creation of tailored 2-D and 3-D nanostructures [7–9], further broadening the potential applications. One of the key areas where magnetic nanomaterials have shown significant potential is in electronics [10–14]. By incorporating these materials into electronic devices, researchers can exploit their static and dynamic magnetization properties [15–18] to enhance the performance and functionality of components such as transistors [14,19] and sensors [12,20,21]. This could lead to the development of faster, smaller, and more efficient electronic devices. In addition to electronics, magnetic nanomaterials hold promise for revolutionizing data storage technologies [22–24]. Due to their ability to store and manipulate magnetic information at the nanoscale, these materials offer the potential for higher storage densities, faster data access speeds, and increased data retention capabilities. This makes them ideal candidates for next-generation magnetic storage devices, such as hard disk drives [25] and magnetic random-access memory (MRAM) [25–27]. Furthermore, magnetic nanomaterials have also attracted attention in the field of biomedical technology [28–30]. Researchers have been exploring their use in various biomedical applications, including targeted drug delivery [31], magnetic resonance imaging (MRI) contrast agents [32], and magnetic hyperthermia for cancer therapy [33,34]. The unique magnetic properties of these materials enable precise control and manipulation at the cellular and molecular levels, opening up new possibilities for diagnostics and therapeutics in medicine.

Nickel (Ni) is a widely studied magnetic material because of its distinctive magnetic properties and the potential for economical large-scale production [35]. It boasts high saturation magnetization (M_s), notable remanence (M_r), and chemical stability. Moreover, its magnetic properties are adjustable based on factors like shape, size, orientation, and surface profile, making it highly versatile for various applications. Additionally, Ni nanoparticles with rough morphology are particularly intriguing due to their elevated surface-to-volume ratio, which enhances catalytic activity and makes them suitable for composite materials. They also exhibit amplified signals in surface-enhanced Raman spectroscopy (SERS) [36,37]. In practical chemical synthesis, Ni nanoparticles often form clusters or chains, where the orientation of these chains within the cluster significantly influences the magnetic response, thus impacting their effectiveness in applications. Therefore, it is essential to gain a comprehensive understanding of the magnetic reversal mechanism in nanochains, focusing particularly on the surface and orientation properties.

In this study, we present the chemical synthesis of Ni nanochains composed of spiky nanostar-shaped particles and examine how their surface roughness and interparticle arrangement influence magnetization reversal. While most earlier studies have investigated reversal in smooth nanostructures such as hexagonal Co platelets or spherical Ni chains [18,38], most simulation work continues to assume idealized geometries with uniform shapes and perfect alignment. Such models often ignore critical features like surface notches, structural irregularities, and misalignments that are inherently present in chemically synthesized systems – limiting the accuracy and relevance of their findings. Our work bridges this gap by systematically varying both the surface spike properties and the degree of chain misalignment, analysing their influence on coercivity (H_C), M_r, and reversal modes through micromagnetic simulations complemented by experiments. We demonstrate that these often-overlooked morphological and structural factors have a significant impact on reversal dynamics, including the emergence of multimodal switching behaviour. By capturing these realistic features, our study provides a more complete understanding of nanomagnetic behaviour, offering valuable insights for future applications in spintronics, neuromorphic computing, biosensors, and soft magnetic devices.

2 Methods

2.1 Experimental

The synthesis of Ni nanoparticles involves a process that yields unique properties and applications in magnetism due to its enhanced surface-to-volume ratio. The production of the Ni nanostar chains can be achieved by the following method, which is illustrated in Figure 1 [38,39]. A solution comprising 45 mM of nickel chloride ($NiCl_2$) dissolved in ethylene glycol is prepared in a cylindrical beaker, followed by the addition of 0.9 M hydrazine hydrate (N_2H_5OH) and 0.1 M sodium hydroxide (NaOH) to the $NiCl_2$ solution. The reaction takes place at a controlled

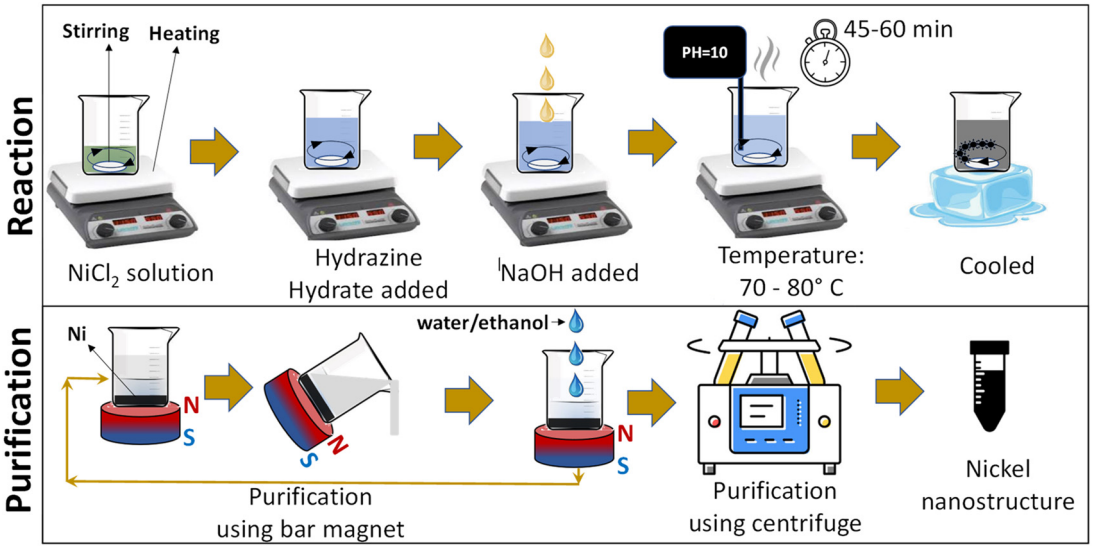

Figure 1: Schematic illustration of the synthesis steps for the nickel (Ni) nanostar chains.

temperature range of 70–80°C, which influences the reaction rate and the size distribution of the resulting nanoparticles. The molar ratio between N_2H_5OH and NaOH is maintained at around 20. Additionally, the pH level of the solution is adjusted to approximately 10. This controlled pH environment provides the optimal conditions for the reaction to progress with desired efficiency. The solution is stirred continuously using a magnetic stirrer at a moderate speed, ensuring coherent rotational motion without inducing turbulence. The stirring produced a gentle, stable vortex, promoting uniform mixing, minimizing shear forces, and aiding in even heat distribution. After approximately 45–60 min of the reaction time, the dark-blue solution gradually transitions to a characteristic grey-black colour. This visual change occurs over a span of several minutes rather than at a distinct moment, serving as a qualitative indicator of Ni nanoparticle synthesis. Near the end of the reduction process, the reaction is gradually terminated by cooling the solution to near 0°C using an ice bath, while continuous stirring is maintained throughout the cooling phase. The synthesis and the cooling process do not employ any external magnetic field, H. From the onset of nucleation, additional Ni atoms are deposited onto existing nuclei, promoting the growth of spherical nanoparticles. As the reaction progresses, nonuniform growth initiates from localized centres on the particle surfaces, giving rise to protrusions or notch-like features, ultimately resulting in star-shaped nanostructures (nanostars). Dipole–dipole interactions among these magnetic nanoparticles promote the self-assembly of interconnected particles. During this process, the particles are suspended in the rotating, viscous solution and undergo circular motion due to continuous stirring. As a result, they experience centrifugal forces proportional to their mass, which dictate their radial positioning within the solution. The synchronized rotation of a large number of similarly sized particles along concentric paths promotes linear aggregation due to the dipolar interaction of the particles, leading to the formation of uniform chain-like assemblies with consistent particle size. With continued deposition, further growth of Ni around these assemblies reinforces and solidifies the chain morphology into a permanent structure. Here, the cooling rate plays a critical role in terminating Ni atom deposition and, consequently, in determining the final shape and morphology of the nanostructures. Rapid or gradual cooling influences how growth fronts are created or suppressed, which directly impacts the formation of distinct nanostructures such as chains or stars.

The subsequent step involves purifying the synthesized nanoparticles. The freshly prepared particles are gently washed multiple times with distilled water and ethanol to remove any unreacted precursors or byproducts. In this process, a bar magnet is used to hold the particles inside the beaker. Following this, the particles are collected *via* centrifugation at 2,000 rpm. After purification, a small volume of highly diluted colloidal solution, containing linear chains of nanostar-shaped particles, is carefully drop-cast onto a pre-cleaned silicon (Si) substrate. These chains initially settle in random orientations on the substrate. An external H of 4 kOe is then applied in-plane using electromagnets. Since the nanochains remain suspended in the colloidal medium, they tend to reorient and align themselves along the direction of the applied H. This leads to partial alignment of the initially disordered chains, as mutual friction restricts free movement. As the solvent gradually evaporates, the field-induced arrangement of the chains is preserved on the substrate.

Regarding the measurement techniques, scanning electron microscopy (SEM) is employed to examine the surface morphology and spatial arrangement of nanostar chain clusters. Energy-dispersive X-ray spectroscopy (EDX) is performed to verify the elemental composition, while magnetic hysteresis characteristics are investigated using a LakeShore 8604 vibrating sample magnetometer (VSM).

2.2 Simulation

In this study, the MuMax[3] micromagnetic simulation technique is utilized to investigate the hysteresis loops and reversal mechanisms of Ni nanostar particles and nanostar chains. The magnetization dynamics is governed by the Landau–Lifshitz–Gilbert (LLG) equation, which describes the precessional motion of magnetization under the influence of the effective magnetic field and damping. The LLG equation is given by $\frac{\partial \boldsymbol{M}}{\partial t} = -\gamma \boldsymbol{M} \times \boldsymbol{H}_{\text{eff}} + \frac{\alpha}{M_s}\left(\boldsymbol{M} \times \frac{\partial \boldsymbol{M}}{\partial t}\right)$, where $\boldsymbol{M}$ is the magnetization vector, γ is the gyromagnetic ratio, $\boldsymbol{H}_{\text{eff}}$ is the effective magnetic field, and α is the Gilbert damping constant. In MuMax[3], the finite difference method (FDM) is utilized to solve the micromagnetic equations governing the behaviour of magnetic materials. FDM discretizes the spatial domain into a grid of points, where the magnetization vector is defined at each grid point. The partial differential equations (LLG equations) are then approximated using finite difference approximations for the spatial derivatives. By iterating over time steps, MuMax[3] computes how the magnetization evolves according to the micromagnetic model, capturing phenomena like domain rotation, magnetic relaxation, and spin dynamics in nanoscale magnetic systems. Our

simulation setup includes Ni nanostar particles and nanostar-chain structures made of particles with varying diameters (D between 70 and 130 nm). Key simulation parameters include $M_s = 4.7 \times 10^5$ A/m, exchange stiffness constant $A_{Ex} = 1.5 \times 10^{-11}$ J/m, $\alpha = 0.9$, magnetocrystalline anisotropy direction along the x (1, 0, 0) axis, and magnetocrystalline anisotropy constant $K_{c1} = -0.5 \times 10^4$ J/m^3. The unit cell size is considered as 3 nm × 3 nm × 3 nm. The nanochains are formed along the x-axis. H is varied in the plane along the x-axis, known as the easy axis; the y-axis, known as the hard axis, and at an angle of 45° with the x-axis to measure the hysteresis loop by recording the average M at each step. The M *versus* H curve provides insights into H_C, M_r, and the overall magnetic behaviour of the system. Analysis of spin configurations at various points along the hysteresis loop reveals the properties of nucleation and propagation of domain walls and other reversal processes in the structure. The hysteresis loop shows typical ferromagnetic features, and the reversal mechanism involves diverse domain wall movements and nucleation events. Our simulations offer a comprehensive understanding of the magnetic behaviour of Ni nanostructures, providing valuable information for designing and optimizing magnetic materials.

3 Results and discussion

3.1 Experimental studies

Figure 2(a) presents an SEM image illustrating the chains of the nanostar particles partially aligned under a H of 4 kOe. These particles, with a median D of 70 nm and about 15% distribution, exhibit a rough surface characterized by distinctive notches. During the chemical synthesis, the particles connect to form straight, rod-like chains, and multiple independent chains assemble into larger clusters. The chains are partially aligned with H during sample preparation, giving the cluster an overall directional characteristic. Due to the mutual friction between the rough surfaces of the chains, their movement in response to H is restricted, resulting in only partial alignment. Achieving perfect alignment would require a stronger H compared to that needed for independent nanoparticles. The inset provides a magnified view of a nanochain, clearly showing the notches that define the surface morphology of the particles. The figure provides a comprehensive visual representation of the nanostar chains and the constituent particles. Figure 2(b) shows EDX results, with peaks corresponding to Ni and Si. The Si peak originates from the Si substrate on which the nanochains are deposited, while the strong presence of Ni peaks confirms that the particles are composed of pure Ni.

Figure 3 illustrates the magnetic hysteresis properties observed in a cluster of nanochains aligned by H. The experimental measurements are conducted on a cluster of nanochain arrays on a Si substrate, where nanostars are constituent particles overlapping each other to form a chain structure. In this setup, the easy axis aligns with the length of the chain, while any direction perpendicular to it represents the hard axis. The schematic diagram in Figure 3(a) represents a single nanostar array consisting of seven particles along with the H configuration. The black arrow running along the length of the chain denotes the easy axis, corresponding to $\phi = 0°$. In contrast, the red arrow perpendicular to it signifies the hard axis, corresponding to $\phi = 90°$, where ϕ denotes the angle between the direction of H

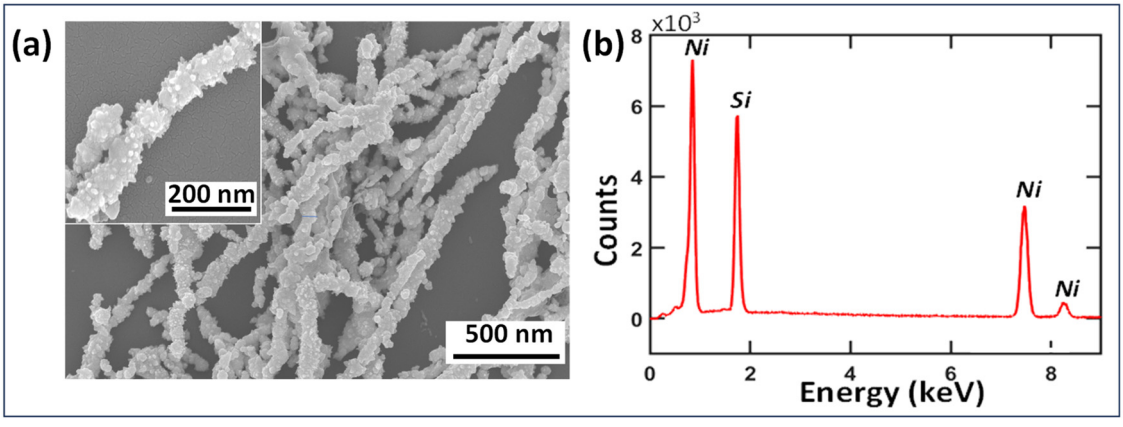

Figure 2: (a) SEM images and (b) EDX analysis of nickel (Ni) nanostar chains. Scale bars for the SEM images are shown in the bottom right corner of each image.

and the easy axis. The curves in the figure illustrate an experimentally observed magnetic hysteresis loop using VSM at ϕ = 0°, 45°, and 90°. The inset shows an enlarged view of the hysteresis curves at H = −1 to 1 kOe, where a significant difference in the curvature of the hysteresis loops is observed. Figure 3(b) shows the H_C and M_r from the loops in Figure 3(a). The H_C values are 0.21, 0.25, and 0.23 kOe for ϕ = 0°, 45°, and 90°, respectively, with no significant variation. The M_r values, defined as the percentage of magnetization remaining relative to the M_S at H = 0 during a hysteresis cycle, are measured to be 38, 29, and 16% for ϕ = 0°, 45°, and 90°, respectively. The M_s remains constant at 4.0 kOe.

The hysteresis loop's nature is rooted in the process of magnetization reversal that can be analysed through the first derivative of the hysteresis loop. The rate of change in the magnetization with field strength is given by the first derivative of the hysteresis curve (dM/dH), which indicates how quickly a material responds to changes in H. The peaks in the differential curves mark regions of pronounced reversal and energy dissipation. A single sharp peak signifies single-domain coherent rotation, indicating high sensitivity and rapid switching. A broad peak or multiple peaks reflect reversal *via* multiple domain formation, with likely pinning centres and vortex formation, leading to low-sensitivity, gradual switching.

In Figure 3(c), differential hysteresis curves (one direction: H negative to positive) are analysed. Each curve displays a single peak that broadens as ϕ increases from 0° to 90°, with the highest peak at 0° gradually diminishing with angle. Figure 3(d) shows the position and width of the peaks in Figure 3(c). The peaks occur at H = 0.25, 0.35, and 0.35 kOe, showing a small variation with ϕ similar to H_c (Figure 3(b)). The full width at half-maximum (FWHM), which measures the width of the curve, increases sharply with ϕ, indicating progressively slower reversal and greater hysteresis loop curvature, consistent with the reduction in M_r (Figure 3(b).

The observed invariance in H_C can be attributed to the presence of a characteristic disorder of the experimental system. In partially aligned nanostar-shaped Ni particle chains, the overall anisotropy is intrinsically weak due to the broad distribution of easy axes for individual chains across the ensemble. Within this framework, notches from the nanostar morphology and misalignments of particles within a chain introduce local shape anisotropy along the

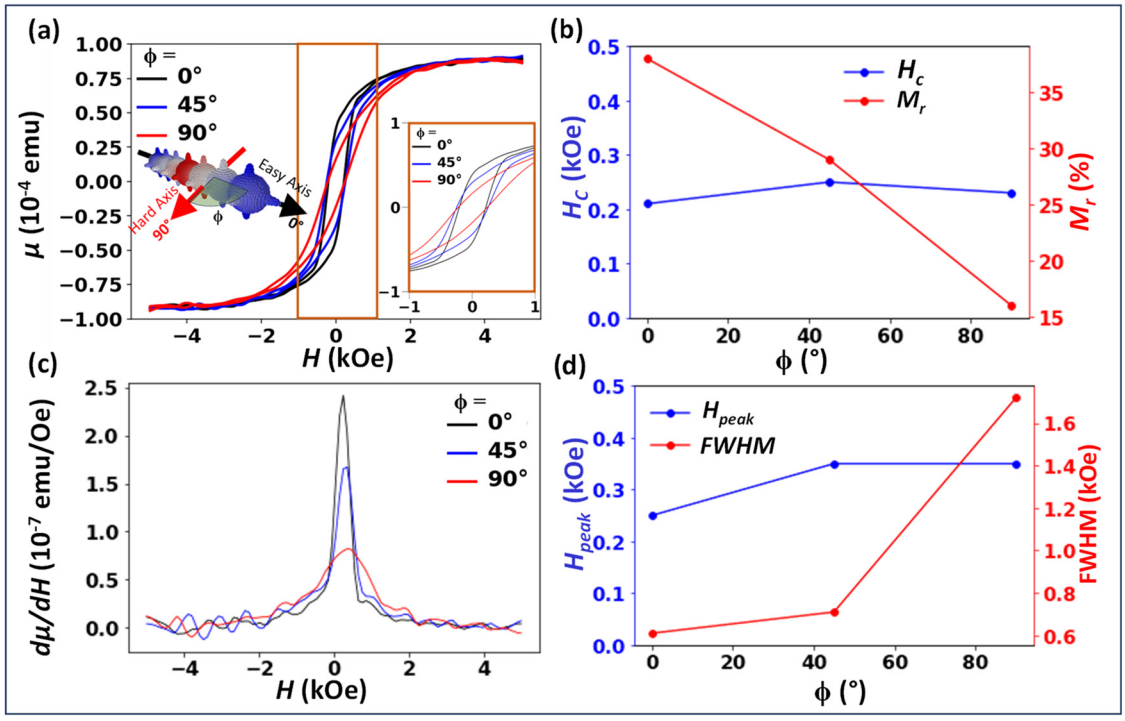

Figure 3: (a) Experimental hysteresis loops (magnetic moment μ *vs* applied magnetic field H) measured at three different field angles (ϕ = 0°, 45°, and 90°). The inset shows an enlarged view of the central region (H = –1 to 1 kOe), and the schematic of the nickel (Ni) nanostar chain illustrates the field orientation used in the measurements. (b) Coercivity (H_c: left y-axis) and remanence (M_r: right y-axis) plotted as a function of ϕ. (c) Differential curves (dμ/dH *vs* H) derived from the one-way hysteresis loops. (d) Peak field (H_{peak}: left y-axis) and FWHM (right y-axis) of the differential curves as a function of ϕ.

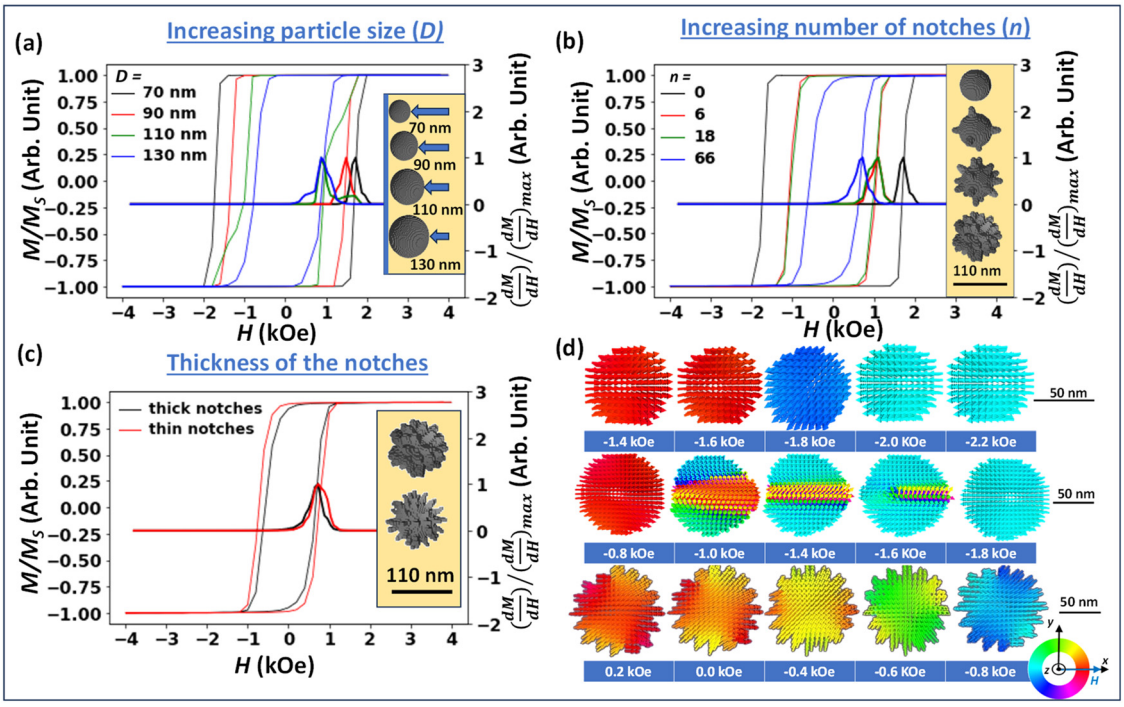

Figure 4: Simulated hysteresis loops (normalized magnetization, M/M_s *vs* magnetic field, H: left y-axis) and differential curves (normalized dM/dH *vs*. H: right y-axis) are shown for single nanoparticles with variations in (a) diameter (D), (b) number of notches (n), and (c) notch width. Panel (d) displays spin configurations at different values of H during magnetization reversal. The top, middle, and bottom rows correspond to nanoparticles of size D = 70, 110, and 70 nm with 20 nm extruded notches, respectively. Scale bars for the structures in each row are shown on the right side of the corresponding row. The colour map and field orientation are located on the bottom right corner.

so-called hard axis, diluting the overall shape anisotropy of the system. Additionally, a large density of structural irregularities, such as notches, bends, shifts, and junctions along the particles, acts as random nucleation centres, where localized domains form and reverse under the influence of edge effects. This mechanism predominantly governs the reversal process, shaping H_C in a manner that is largely independent of the rotation angle. The simulation study presented in Figure 5 further supports the invariance of H_c with ϕ in a disordered system, as discussed later in the paper.

This variation in the loop curvature, on the other hand, arises from the demagnetizing energy (E_D), which originates from dipole–dipole interactions [40,41] between the particles. At ϕ = 90°, the magnetization lies perpendicular to the chain length, leading to a larger stray field leakage and a higher E_D. These stray fields are spatially nonuniform and couple through dipole–dipole interactions along the particle chain. The resulting internal fields oppose the applied field, causing different spins or particle segments to experience different effective fields. This promotes gradual, noncoherent rotation rather than sharp switching. In contrast, at ϕ = 0°, E_D is lower and the stray field is weaker because the spins largely align with the anisotropy direction. Reversal then proceeds through domain wall rotation with minimal influence from the stray field effect.

3.2 Simulation studies

3.2.1 Single particles

Understanding the behaviour of a single particle is essential for explaining the dynamics of nanochain clusters. Figure 4(a) shows the hysteresis loops that individual spherical particles of different sizes exhibit. As the size increases, H_c decreases. Spherical particles with D = 70 nm display the widest square-shaped loop, with H_C = 1.72 kOe. For D = 90 nm, the loop becomes narrower with H_C = 1.41 kOe. At D = 110 nm, a step-like reversal appears, with H_C = 0.96 kOe. Increasing the size further to D = 130 nm results in a more gradual and narrower loop with H_C = 0.83 kOe. As the particle diameter increases, the normalized differential curve undergoes notable changes. The single peaks shift to lower fields and broaden, with broadening measured by FWHM or, more effectively, for nonuniform peaks; in this case, by the area under the curve (A).

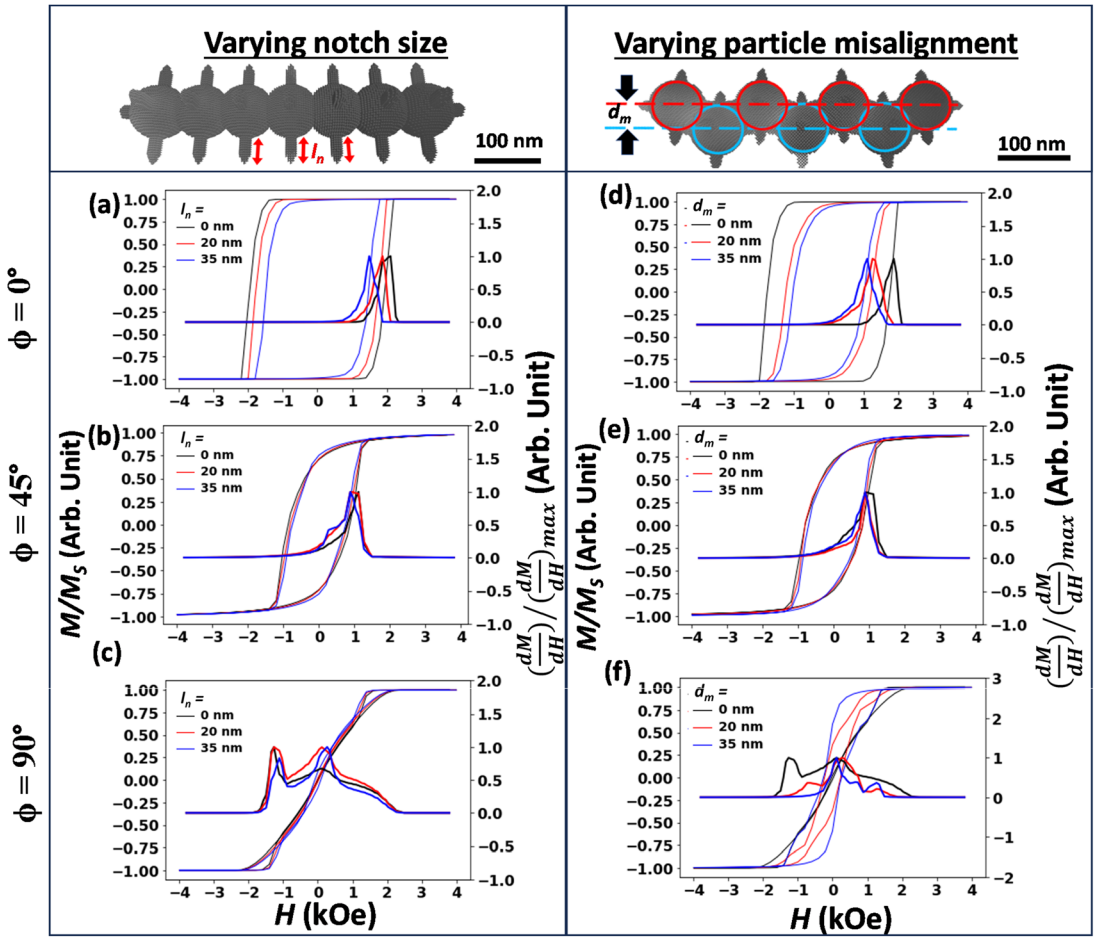

Figure 5: Simulated hysteresis loops (left *y*-axis) and corresponding differential hysteresis curves (right *y*-axis) for a single nanostar chain composed of seven particles. Panels (a)–(c) show the effect of varying notch size (l_n), while panels (d)–(f) illustrate the effect of misalignment between neighbouring particles (d_m). In each panel, the black, red, and blue curves represent field angles ϕ = 0°, 45°, and 90°, respectively.

The shift indicates that the highest rate of magnetization reversal occurs at lower fields, consistent with a reduction in H_C. The increase in A corresponds to peak broadening, implying that energy dissipation is distributed over a wider field range. For particles with D = 70 nm, a single sharp peak is observed, with the smallest A (= 263 in arbitrary units), suggesting the presence of a single-domain structure. At D = 90 nm, the peak broadens (A = 302), indicating a loss of coherence and deviation from ideal single-domain behaviour. For D = 110 nm, a clear additional peak emerges at a higher field (A = 323), signifying the formation of at least two domains. Finally, D = 130 nm exhibits the broadest peak (A = 423), as reversal spans a wide field range, implying multiple domain formation and a complete loss of coherence. The E_D, a key component of the magnetic energy landscape, plays a significant role in interpreting the results presented in Figure 4(a). At the saturation field, E_D is determined to be 7.9 × 10^{-18}, 1.7 × 10^{-17}, 3.1 × 10^{-17}, and 5.1 × 10^{-17} J for D = 70, 90, 110, and 130 nm, respectively, exhibiting a monotonic increase with particle size.

Figure 4(b) presents the findings concerning the augmentation of the number of notches (n) on a spherical particle. The diameter of the core is set at 70 nm, and the notches extend 20 nm beyond the sphere's surface. Four scenarios are explored, featuring n = 0, 6, 18, and 66 notches, respectively. These notches exhibit symmetry along the x, y, and z axes. In the initial scenario, a 70 nm nanosphere is considered. In the second case, cones are affixed atop the core along the ±x, ±y, and ±z axes to form a total of 6 notches. In the subsequent (third) scenario, 18 notches are achieved by rotating and overlaying the first configuration by 45° along each axis. Similarly, the third configuration is rotated by 22.5° along all three axes to yield the final configuration, featuring 66 notches. The result is similar to increasing the size of the particle. With

the increasing number of notches, H_C reduces, and the broadening of the differential curve occurs, referring to single-to-multiple-domain formation. As the density of notches increases, the structure coincides with the 110 nm sphere. However, H_C is smaller, and the differential curve is wider for the notched particles as compared to the 110 nm spherical particle, indicating the role of surface roughness in domain nucleation, which aids multidomain creation. In this system, E_D is measured to be 7.9×10^{-18}, 8.3×10^{-18}, 8.8×10^{-18}, and 1.1×10^{-17} J for 0, 6, 18, and 66 notches, respectively. Figure 4(c) compares the thick to thin notch size. H_C is larger, and the peak is broader for the thinner notches. This indicates that the pinning of domains is more pronounced for thinner notches.

Figure 4(d) illustrates the magnetization reversal mechanisms through spin configurations and colour mapping at H for three distinct samples. The first sample is a D = 70 nm solid sphere, the second is a D = 110 nm solid sphere, and the third is a notched nanoparticle with D = 70 nm cores and 20 nm notches. The spin configurations shown represent the cross-sectional view of the diameter in the x–y plane. In the first case, the spins rotate coherently from left to right. In the second case, we observe the formation of three distinct reversal domains (H = −1.0 kOe), creating a twisted spin structure. The upper half of the image shows an in-plane anticlockwise rotation, the bottom half shows an in-plane clockwise rotation, and the central part exhibits a vertical (out-of-plane) reversal. This indicates that a single particle demonstrates three different domain wall reversals: two in-plane with opposite chirality and one out-of-plane. The in-plane domain reversal occurs earlier, while the out-of-plane domains take longer to reverse. Initially, the central region resists reversal, but gradually the domain size decreases and eventually reverses through an out-of-plane rotation. In the third scenario, the reversal mechanism is influenced by the size of the notches. The notches aid the formation of smaller local domains, promoting the multidomain feature of reversal.

The reversal characteristics of a single particle observed in this section can be interpreted through several foundational works [42,43]. Based on the size, two different types of distinct reversal mechanisms can be observed in nanoparticles. For particles smaller than the critical diameter D_c, reversal occurs through coherent spin rotation within a single domain. The reversal is thermally activated over an anisotropy energy barrier that scales with particle volume, causing H_C to increase with size up to D_c. When the particle size exceeds D_c, multidomain states become energetically favourable. In this multidomain regime, H_C decreases with size because, with a larger number of domains, reversal is energetically less costly than coherent rotation. In this regime, domains reverse independently at different field values, producing a gradual hysteresis loop and broadening of the differential curve. From the hysteresis loops (Figure 4(a)) and domain analysis (Figure 4(d)), only the 70 nm particle shows single-domain-like behaviour, while larger sizes display multidomain reversal, with the study range lying near the single-domain critical diameter and extending to the fully multidomain regime. E_D increases with the particle size because larger particles generate more extensive stray fields that enhance long-range dipole–dipole coupling, facilitating the destabilization of single-domain configurations and multidomain formation. This, in turn, reduces the field required for reversal. The observed monotonic decrease in H_C and an increase in A under the differential curve with increasing particle size are consistent with multidomain behaviour.

In Figure 4(b), the increase in E_D from smooth to notched nanospheres is due to both geometric effects and stronger dipole–dipole interactions [40,41]. Surface notches or spikes increase the effective surface area and create regions of high curvature with locally concentrated magnetic charges, producing stronger, more nonuniform stray fields. This elevates local E_D with notches that serve as preferential nucleation sites for reversal, allowing domain walls to propagate more readily and lowering coercivity. Smooth nanospheres lack these features, resulting in more coherent reversal and higher switching fields.

3.2.2 Single chains

Figure 5 shows simulated hysteresis loops for seven-particle (D = 70 nm) chains. Figure 5(a–c) illustrates particle-level surface disorder from varying notch sizes (l_n = 0, 20, and 35 nm; n = 6), while Figure 5(d–f) depicts chain-level misalignment disorder, where alternate particle centres are periodically displaced by d_m rather than all aligned along the chain's long axis (d_m = 0, 20, and 35 nm; l_n = 20 nm and n = 6). The top row (Figure 5(a) and (d)), middle row (Figure 5(b) and (e)), and bottom row (Figure 5(c) and (f)) correspond to ϕ = 0° (easy axis), 45°, and 90° (hard axis), respectively. The black hysteresis loops in Figure 5(a)–(c) (without notches), and Figure 5(d)–(f) (aligned chains) represent the reference structures for comparing the effects of particle roughness and chain misalignment on the reversal process.

Figure 5(a) shows hysteresis loops with H_C decreasing and notch size (l_n) increasing, indicating strong anisotropy along the long axis and easier switching with larger notches. The differential curves display single peaks (broader than

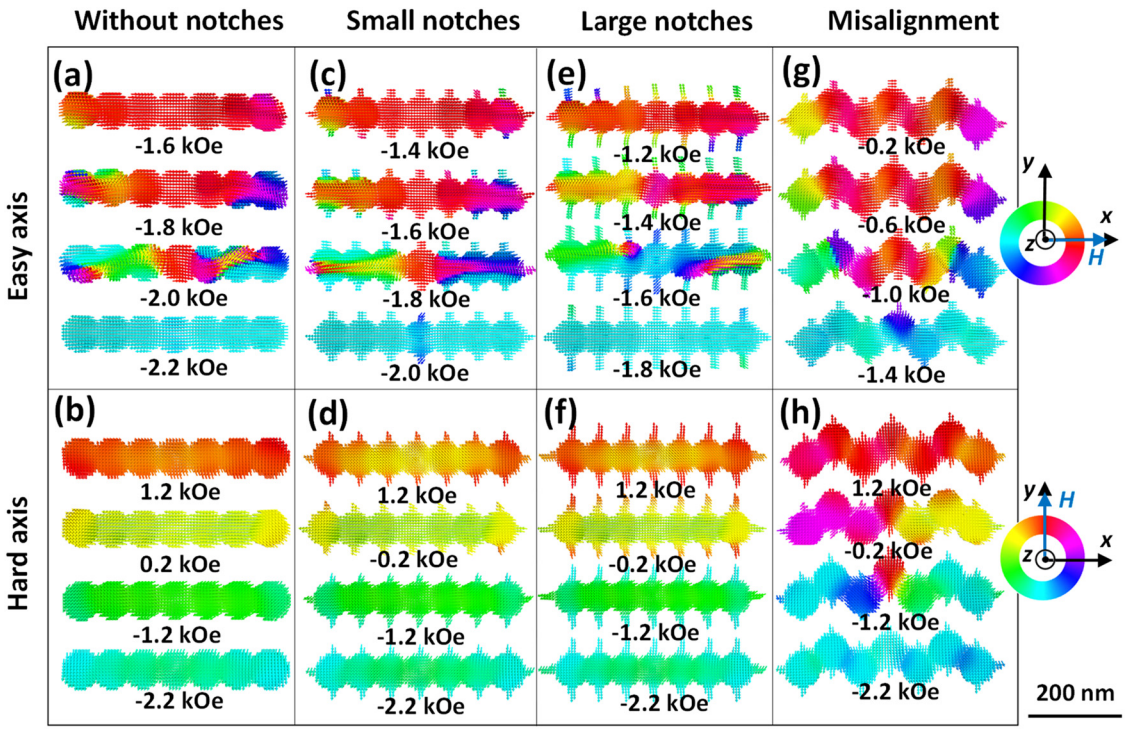

Figure 6: Simulated magnetization reversal behaviour of a single nanostar chain consisting of seven particles, each with a diameter D = 70 nm. Panels (a) and (b) show particles without notches; (c) and (d) with notch length l_n = 20 nm; (e) and (f) with notch length l_n = 35 nm; and (g) and (h) with particle misalignment d_m = 35 nm. Panels (a), (c), (e), and (g), and (b), (d), (f), and (h) represent magnetization reversal along the easy and hard axes, respectively. The colour maps and field orientations for each panel row are shown on the right side of the corresponding row. Scale bars for the structures are provided in the bottom right corner of the figure.

individual particles) shifting to lower fields as the loops narrow, with A decreasing from 494 at l_n = 0 to 442 at l_n = 20 nm and 448 at l_n = 35 nm, suggesting slightly more coherent reversal for particles with larger notches. In Figure 5(b), the loops are more curved, with H_C and M_r markedly lower than those in Figure 5(a) and unaffected by the notch size. The differential curves broaden compared to Figure 5(a) and develop additional modes, indicating multiple switching mechanisms. Figure 5(c) shows negligible H_C and M_r for the hard-axis loops, indicating a less energetically demanding reversal. The wider differential curves display two distinct modes, reflecting less uniform switching and two magnetization processes with a relative phase of rotation. Notches alter the relative intensities of these modes without shifting their positions, affecting the mode strength distribution but not the modes themselves. A comparison of Figure 5(a) and (c) shows that the contrast in H_C between the easy and hard axes diminishes with the introduction of notch disorder, solely due to the reduction of H_C along the easy axis relative to the reference structure.

The variation in particle misalignment (Figure 5(d)–(f)) produces effects on the hysteresis curves somewhat similar to those from varying notches (Figure 5(a)–(c)), including a reduction in H_C with increasing misalignment disorder along the easy axis (Figure 5(d)) and a decrease in H_C with increasing ϕ toward the hard axis (Figure 5(d)–(f)). However, notable differences emerge between the two disorder types. For the easy-axis case, unlike the notch disorder in Figure 5(a), the misalignment disorder in Figure 5(d) introduces curvature in the loop (A = 442, 650, 622 for d_m = 0, 20, and 35 nm, respectively). For the hard-axis case, the notch disorder in Figure 5(c) yields negligible H_C and M_r, with no significant variation across disorder magnitudes. In contrast, misalignment disorder in Figure 5(f) produces marked changes, with H_C increasing up to 0.26 kOe and M_r zooms up to 56% from near-zero reference values. The differential curve shows complex behaviour, with multiple modes whose peak positions shift as alignment is disturbed, indicating that reversal modes are redefined independently in each case without apparent correlation. A comparison of Figure 5(d) and (f) shows that misalignment disorder greatly reduces the H_C contrast between easy and hard axes, driven by both reduced H_C along the easy axis and enhanced H_C along the hard axis relative to the reference structure. The reduced contrast of H_C between the easy and hard axes under notch and

misalignment disorder discussed in Figure 5 indicates that, in the experimental system of nanostar-particle chains, multi-scale disorder significantly suppresses the angular dependence of H_C, as observed in Figure 3(b).

Figure 6 illustrates the spin configuration during the magnetization reversal process of nanochain structures, with colour mapping representing the in-plane angle of the magnetization vector. The four columns, from left to right, correspond to seven-particle aligned nanochains (D = 70 nm) without notches, with smaller notches (l_n = 20 nm and n = 6), larger notches (l_n = 35 nm and n = 6), and a chain with misaligned particles (d_m = 20 nm, l_n = 20 nm and n = 6). The top and bottom rows correspond to reversal along the easy and hard axes, respectively. The colour convention for the magnetization spin configurations along with field orientation is displayed on the right side of each row.

In Figure 6(a), for the chain without notches and with the field applied along the easy axis, the reversal nucleates at the two ends of the chain. Within a short field range, it progresses inward in a spiral motion, ultimately reversing the central part. Figure 6(b) illustrates the reversal along the hard axis, occurring over a much wider field range. In the figure, at least two reversal mechanisms are observed: a smaller group of spins in the central part starts reversing earlier and finishes later, resulting in two distinct modes. With the introduction of notches in the hard-axis loop (Figure 6(d) and (f)), the share of the minority spins zooms, resulting in the variation in the intensity of the modes. The reversal in Figure 6(c) and (e) demonstrates easy-axis coherent rotation similar to Figure 6(a), but the dynamics differ in the presence of notches. In Figure 6(c), the reversal starts at the notches on the particles at the ends of the chain, then propagates through the volume of the particles, and finally, reaches the central particle. In contrast, Figure 6(e) shows that the reversal of the central particle occurs earlier, highlighting the significant role notches play in controlling reversal dynamics. The reversal of misaligned chains in the easy- and hard-axis geometry is significantly different from that in aligned chains. In both cases, a complex reversal process is observed, involving the formation of multiple domains initiated by each overlapping region of the misaligned particles (Figure 6(g) and (h)). When comparing reversals between easy and hard axes, they show more similarities than aligned ones, both with and without notches. This is also evidenced by the reduced H_C in the easy-axis hysteresis curve and increased H_C in the hard-axis hysteresis curve, as shown in Figure 5(d) and (f), making the loops more comparable. This misalignment effect can be utilized to make the reversal process of a system more uniform across any applied field angles.

A comparison between the experimental and simulation studies reveals that both approaches demonstrate complex domain dynamics during the reversal process, with noticeable variations in the hysteresis loop properties as a function of the field angle, showing consistent trends across both methods. The experimental sample comprises a large number of chains of nanostar particles, each featuring many notch-like protrusions, partially aligned on a 10 nm × 10 nm substrate. Given the constraints of time and computational capacity, replicating every microscopic detail of the experimental sample in simulations is impractical. Instead, key structural features, such as the particle size, notch density, notch dimensions, and particle misalignment within the chains are analysed to understand the reversal mechanism by tracking changes in spin configuration throughout a hysteretic cycle. Theoretical studies reveal that the presence of notches reduces coercivity in the easy axis, while disorders lead to an increased similarity between the easy- and hard-axis hysteresis loops. The findings align well with experimental observations.

4 Conclusions

In conclusion, this study provides an in-depth analysis of the size and surface features of Ni nanoparticles and the alignment characteristics of chains composed of connected nanostar particles, focusing on their impact on magnetization reversal dynamics. Experimental and simulation studies of hysteresis loops and reversal mechanisms are conducted for nanoparticle assembly across various field angles and geometric configurations. Special emphasis is placed on the role of surface roughness featured by symmetrically distributed notches on spherical particles, and the effect of breaking the coaxial alignment of nanochains by introducing an off-axis shift to alternate particles. A detailed investigation is carried out to examine how the notches and misalignments affect the magnetization behaviour of the system. The analysis reveals significant changes in the hysteresis characteristics, as evidenced by variations in both the hysteresis and differential hysteresis curves. Magnetic parameters, like coercivity, remanence, and features of the differential modes, exhibit notable alterations. Additionally, interesting variations in the magnetization reversal mechanisms are observed, indicating a strong sensitivity to structural and geometric properties of nanostar particles/chains. This study significantly advances the understanding of magnetization reversal dynamics in nanoparticle systems by considering more realistic surface and geometric features found in

chemically synthesized particles. This improved understanding enhances control over their properties and supports a wide range of nanotechnology applications.

Acknowledgments: This work was supported by research funding from Khalifa University (CIRA 2021-071, project code: 8474000416), National Research Foundation (NRF), Singapore, for grant NRF-CRP21-2018-003, and research funding from SRMIST (SRMIST/R/AR(A)/SERI2024/174/41/342).

Funding information: This work was supported by research funding from Khalifa University (CIRA 2021-071, project code: 8474000416), National Research Foundation (NRF), Singapore, for grant NRF-CRP21-2018-003, and research funding from SRMIST (SRMIST/R/AR(A)/SERI2024/174/41/342).

Author contributions: All authors have accepted responsibility for the entire content of this manuscript and approved its submission.

Conflict of interest: The authors state no conflict of interest.

Data availability statement: All data generated or analysed during this study are included in this published article.

References

[1] Barman A, Mondal S, Sahoo S, De A. Magnetization dynamics of nanoscale magnetic materials: A perspective. J Appl Phys. 2020;128(17):170901.
[2] Rana B, Mondal AK, Bandyopadhyay S, Barman A. Applications of nanomagnets as dynamical systems: I. Nanotechnology. 2021;33(6):062007.
[3] Kasani S, Curtin K, Wu N. A review of 2D and 3D plasmonic nanostructure array patterns: fabrication, light management and sensing applications. Nanophotonics. 2019;8(12):2065–89.
[4] Das G, Battista E, Manzo G, Causa F, Netti PA, Di Fabrizio E. Large-scale plasmonic nanocones array for spectroscopy detection. ACS Appl Mater Interfaces. 2015;7(42):23597–23604.
[5] Barman A, Gubbiotti G, Ladak S, Adeyeye AO, Krawczyk M, Gräfe J, et al. The 2021 magnonics roadmap. J Phys: Condens Matter. 2021;33(41):413001.
[6] de Aberasturi DJ, Serrano-Montes AB, Liz-Marzán LM. Modern applications of plasmonic nanoparticles: from energy to health. Adv Opt Mater. 2015;3(5):602–17.
[7] Ganguly A, Zafar H, Howells CT, Pereira MF, Das G. Controlling vertical asymmetry of nanocrystals through anisotropic etching-assisted nanosphere lithography. Small Struct. 2024;5(3):2300300.
[8] Ganguly A, Das G. Stretching the horizon of nanosphere lithography. In: Dipti Ranjan S, editor. Nanofabrication techniques. Rijeka: IntechOpen; 2023. p. Ch. 7.
[9] Ganguly A, Das G. Combining azimuthal and polar angle resolved shadow mask deposition and nanosphere lithography to uncover unique nano-crystals. Nanomaterials. 2022;12(19):3464.
[10] Singamaneni S, Bliznyuk VN, Binek C, Tsymbal EY. Magnetic nanoparticles: recent advances in synthesis, self-assembly and applications. J Mater Chem. 2011;21(42):16819–45.
[11] Lisjak D, Mertelj A. Anisotropic magnetic nanoparticles: A review of their properties, syntheses and potential applications. Prog Mater Sci. 2018;95:286–328.
[12] Gloag L, Mehdipour M, Chen D, Tilley RD, Gooding JJ. Advances in the application of magnetic nanoparticles for sensing. Adv Mater. 2019;31(48):1904385.
[13] Crisan O, Crisan A, Dumitrache F, Luculescu C. Hybrid nanoelectronic-magnetic device with magnetoresistive core–shell Fe/FeC nanoparticles. Appl Phys A. 2020;126(3):200.
[14] Bedanta S, Barman A, Kleemann W, Petracic O, Seki T. Magnetic nanoparticles: a subject for both fundamental research and applications. J Nanomater. 2013;2013(1):952540.
[15] Ganguly A, Zhang S, Miron IM, Kosel J, Zhang X, Manchon A, et al. Competition between chiral energy and chiral damping in the asymmetric expansion of magnetic bubbles. ACS Appl Electron Mater. 2021;3(11):4734–42.
[16] Barman S, Ganguly A, Barman A. Configuration and polarization dependent transverse domain wall motion and domain wall switching in ferromagnetic nanowire. Spin. 2013;3:1350001.
[17] King J, Ganguly A, Burn D, Pal S, Sallabank E, Hase T, et al. Local control of magnetic damping in ferromagnetic/non-magnetic bilayers by interfacial intermixing induced by focused ion-beam irradiation. Appl Phys Lett. 2014;104(24):242410.
[18] Mahato B, Ganguly A, Rana B, Barman A. Magnetization reversal in chemically synthesized hexagonal cobalt microplatelets. J Phys Chem C. 2012;116(41):22057–62.
[19] Bogani L, Maurand R, Marty L, Sangregorio C, Altavilla C, Wernsdorfer W. Effect of sequential grafting of magnetic nanoparticles onto metallic and semiconducting carbon-nanotube devices: towards self-assembled multi-dots. J Mater Chem. 2010;20(11):2099–107.
[20] Jiang B, Lian L, Xing Y, Zhang N, Chen Y, Lu P, et al. Advances of magnetic nanoparticles in environmental application: environmental remediation and (bio) sensors as case studies. Environ Sci Pollut Res. 2018;25:30863–79.
[21] Koh I, Josephson L. Magnetic nanoparticle sensors. Sensors. 2009;9(10):8130–45.
[22] Mendonsa R, Liang S, Wang J-P. Magnetic nanoparticles (MNPs) based on additively manufactured memory devices. AIP Adv. 2024;14(2):025205.
[23] Koplovitz G, Primc D, Ben Dor O, Yochelis S, Rotem D, Porath D, et al. Magnetic nanoplatelet-based spin memory device operating at ambient temperatures. Adv Mater. 2017;29(17):1606748.
[24] Jung JH, Kim S, Kim H, Park J, Oh JH. High-performance flexible organic nano-floating gate memory devices functionalized with cobalt ferrite nanoparticles. Small. 2015;11(37):4976–84.
[25] Nallusamy S, Venkidusamy V, Chidhambaram N, Pabba DP, Shanavas S, Thirumurugan A. Functionalized magnetic nanomaterials for data storage applications. In Nanostructured magnetic materials. Boca Raton, Florida, USA: CRC Press; 2023. p. 255–79.
[26] Mitra A, Mohapatra J, Aslam M. Magnetic and electronic properties of anisotropic magnetite nanoparticles. Mater Res Express. 2024;11(2):022002.
[27] Hai PN, Tanaka M. Memristive magnetic tunnel junctions with MnAs nanoparticles. Appl Phys Lett. 2015;107(12):122404.

[28] Berry CC, Curtis AS. Functionalisation of magnetic nanoparticles for applications in biomedicine. J Phys D: Appl Phys. 2003;36(13):R198.
[29] Pankhurst Q, Thanh N, Jones S, Dobson J. Progress in applications of magnetic nanoparticles in biomedicine. J Phys D: Appl Phys. 2009;42(22):224001.
[30] Selim MM, El-Safty S, Tounsi A, Shenashen M. A review of magnetic nanoparticles used in nanomedicine. APL Mater. 2024;12(1):010601.
[31] Kianfar E. Magnetic nanoparticles in targeted drug delivery: a review. J. Supercond. Nov Magn. 2021;34(7):1709–35.
[32] Issa B, Obaidat IM. Magnetic nanoparticles as MRI contrast agents. Magn Reson Imaging. 2019;378(40):10.5772.
[33] Włodarczyk A, Gorgoń S, Radoń A, Bajdak-Rusinek K. Magnetite nanoparticles in magnetic hyperthermia and cancer therapies: Challenges and perspectives. Nanomaterials. 2022;12(11):1807.
[34] Farzin A, Etesami SA, Quint J, Memic A, Tamayol A. Magnetic nanoparticles in cancer therapy and diagnosis. Adv Healthc Mater. 2020;9(9):1901058.
[35] Davar F, Fereshteh Z, Salavati-Niasari M. Nanoparticles Ni and NiO: synthesis, characterization and magnetic properties. J Alloy Compd. 2009;476(1–2):797–801.
[36] Wang L, Wang Z, Li L, Zhang J, Liu J, Hu J, et al. Magnetic–plasmonic Ni@ Au core–shell nanoparticle arrays and their SERS properties. RSC Adv. 2020;10(5):2661–9.
[37] Fu Q, Wong KM, Zhou Y, Wu M, Lei Y. Ni/Au hybrid nanoparticle arrays as a highly efficient, cost-effective and stable SERS substrate. RSC Adv. 2015;5(8):6172–80.
[38] Rana B, Ganguly A, Barman A. Magnetic shape anisotropy in chemically synthesized chains of nickel nanoparticles. IEEE Trans Magn. 2011;47(10):2859–62.
[39] Wu S-H, Chen D-H. Synthesis and characterization of nickel nanoparticles by hydrazine reduction in ethylene glycol. J Colloid Interface Sci. 2003;259(2):282–6.
[40] Bandyopadhyay M, Dattagupta S. Memory in nanomagnetic systems: Superparamagnetism *versus* spin-glass behavior. Phys Rev B. 2006;74(21):214410.
[41] Chakraverty S, Bandyopadhyay M, Chatterjee S, Dattagupta S, Frydman A, Sengupta S, et al. Memory in a magnetic nanoparticle system: Polydispersity and interaction effects. Phys Rev B. 2005;71(5):054401.
[42] Chakraverty S, Bandyopadhyay M. Coercivity of magnetic nanoparticles: a stochastic model. J Phys: Condens Matter. 2007;19(21):216201.
[43] Sung Lee J, Myung Cha J, Young Yoon H, Lee J-K, Keun Kim Y. Magnetic multi-granule nanoclusters: A model system that exhibits universal size effect of magnetic coercivity. Sci Rep. 2015;5(1):12135.